Impact of JPEG2000 Compression on Spatial-Spectral Endmember Extraction from Hyperspectral Data

Gabriel Martín[a], V. G. Ruiz[b], Antonio Plaza[a], Juan P. Ortiz[b], Inmaculada García[b]

[a]Dept. Tecnología de Computadores y Comunicaciones, Univ. Extremadura Avda. de la Universidad s/m, E-10071 Cáceres, Spain;
[b]Dept. Arquitectura de Computadores y Electrónica, Univ. Almería Ctra. Sacramento s/n, La Cañada de San Urbano, E-04120 Almería, Spain

ABSTRACT

Hyperspectral image compression has received considerable interest in recent years. However, an important issue that has not been investigated in the past is the impact of lossy compression on spectral mixture analysis applications, which characterize mixed pixels in terms of a suitable combination of spectrally pure spectral substances (called *endmembers*) weighted by their estimated fractional abundances. In this paper, we specifically investigate the impact of JPEG2000 compression of hyperspectral images on the quality of the endmembers extracted by algorithms that incorporate both the spectral and the spatial information (useful for incorporating contextual information in the spectral endmember search). The two considered algorithms are the automatic morphological endmember extraction (AMEE) and the spatial spectral endmember extraction (SSEE) techniques. Experimental results are conducted using a well-known data set collected by AVIRIS over the Cuprite mining district in Nevada and with detailed ground-truth information available from U. S. Geological Survey. Our experiments reveal some interesting findings that may be useful to specialists applying spatial-spectral endmember extraction algorithms to compressed hyperspectral imagery.

Keywords: Hyperspectral image compression, JPEG2000, spatial-spectral endmember extraction, spectral unmixing, automatic morphological endmember extraction (AMEE), spatial spectral endmember extraction (SSEE).

1. INTRODUCTION

Hyperspectral image compression[1] has received considerable interest in recent years due to the enormous data volumes collected by imaging spectrometers such as NASA's Airborne Visible Infra-Red Imaging Spectrometer (AVIRIS),[2] which is now able to cover the wavelength region from 0.4 to 2.5 microns using more than 200 spectral channels, at nominal spectral resolution of 10 nm. Two types of image compression have been applied in hyperspectral imaging applications: lossless and lossy. Since the best compression ratios achieved by lossless methods are in the order of 3:1, lossy decodings are used when higher compression ratios are required.[3]

An important issue that has not been investigated in the past is the impact of lossy compression on spectral unmixing applications,[4] which are the tool of choice in order to deal with the phenomenon of mixed pixels,[5] i.e. pixels containing different macroscopically pure spectral substances (*endmembers*) which can be unmixed by establishing a suitable combination of endmembers, weighted by their estimated fractional abundances. In the last few years, several algorithms have been proposed for automatic extraction of spectral endmembers.[6] Classic techniques have been mostly focused on exploiting the spectral information contained in the data. However, one of the distinguishing properties of hyperspectral data is the multivariate information coupled with a two-dimensional (pictorial) representation amenable to image interpretation. Subsequently, endmember extraction algorithms can benefit from an integrated framework in which both the spectral information and the spatial arrangement of pixel vectors are taken into account. To the best of our knowledge, only a few attempts exist in the literature aimed at including the spatial information in the process of extracting spectral endmembers. Two of the most representative ones are the automatic morphological endmember extraction (AMEE)[7] and the spatial spectral endmember extraction (SSEE)[8] algorithm.

In this work, we investigate the impact of JPEG2000[9] compression of the original hyperspectral scene on the quality of the endmembers and fractional abundances derived after using AMEE and SSEE algorithms. In

Satellite Data Compression, Communication, and Processing V, edited by Bormin Huang, Antonio J. Plaza, Raffaele Vitulli,
Proc. of SPIE Vol. 7455, 74550A · © 2009 SPIE · CCC code: 0277-786X/09/$18 · doi: 10.1117/12.826318

experiments, we use a well-known hyperspectral data set collected by AVIRIS over the Cuprite mining district in Nevada and with detailed ground-truth information available from U. S. Geological Survey. The remainder of the paper is structured as follows. Section 2 formulates the spectral unmixing problem addressed in this work and further describes the two considered spatial-spectral endmember extraction algorithms. Section 3 describes the JPEG2000 standard adopted in our data compression experiments. In Section 4 the wavelet filters used in our experiments are presented. Section 5 describes the AVIRIS hyperspectral image data set used in experiments and further provides an experimental evaluation on the impact of data compression on the considered algorithms. Finally, section 6 concludes the paper with some remarks and hints at plausible future research lines.

2. SPATIAL-SPECTRAL ENDMEMBER EXTRACTION AND UNMIXING

Let us assume that a remotely sensed hyperspectral scene with n bands is denoted by $\mathbf{I}$, in which the pixel at the discrete spatial coordinates (i, j) of the scene is represented by a vector $\mathbf{X}(i, j) = [x_1(i, j), x_2(i, j), \cdots, x_n(i, j)] \in \Re^n$, where $\Re$ denotes the set of real numbers in which the pixel's spectral response $x_k(i, j)$ at sensor channels $k = 1, \ldots, n$ is included. Under the linear mixture model assumption, each pixel vector in the original scene can be modeled using the following expression:

$$\mathbf{X}(i, j) = \sum_{z=1}^{p} \Phi_z(i, j) \cdot \mathbf{E}_z + \mathbf{n}(i, j), \tag{1}$$

where $\mathbf{E}_z$ denotes the spectral response of endmember z, $\Phi_z(i, j)$ is a scalar value designating the fractional abundance of the endmember z at the pixel $\mathbf{X}(i, j)$, p is the total number of endmembers, and $\mathbf{n}(i, j)$ is a noise vector. The solution of the linear spectral mixture problem described in (1) relies on a successful estimation of how many endmembers, p, are present in the input hyperspectral scene $\mathbf{I}$, and also on the correct determination of a set $\{\mathbf{E}_z\}_{z=1}^{p}$ of endmembers and their correspondent abundance fractions $\{\Phi_z(i, j)\}_{z=1}^{p}$ at each pixel $\mathbf{X}(i, j)$. Two physical constrains are generally imposed into the model described in (1), these are the abundance non-negativity constraint (ANC), i.e., $\Phi_z(i, j) \geq 0$, and the abundance sum-to-one constraint (ASC), i.e., $\sum_{z=1}^{p} \Phi_z(i, j) = 1$.[10]

Over the last decade, several algorithms have been developed for automatic or semi-automatic extraction of spectral endmembers.[6] Classic techniques include the pixel purity index (PPI),[11] N-FINDR,[12] iterative error analysis (IEA),[13] optical real-time adaptive spectral identification system (ORASIS),[14] convex cone analysis (CCA),[15] and an orthogonal subspace projection (OSP) technique.[16] Other advanced techniques for endmember extraction have been recently proposed,[6] but very few of them consider spatial adjacency. However, one of the distinguishing properties of hyperspectral data is the multivariate information coupled with a two-dimensional (pictorial) representation amenable to image interpretation. Subsequently, most endmember extraction algorithms listed above could benefit from an integrated framework in which both the spectral information and the spatial arrangement of pixel vectors are taken into account. To the best of our knowledge, only a few attempts exist in the literature aimed at including the spatial information in the process of extracting spectral endmembers. Two of the most representative efforts in this direction are described below:

- The automatic morphological endmember extraction (AMEE)[7] algorithm runs on the full data cube with no dimensional reduction, and begins by searching spatial neighborhoods around each pixel in the image for the most spectrally pure and mostly highly mixed pixel. This task is performed by using extended mathematical morphology operators[17] of dilation and erosion, respectively. Each spectrally pure pixel is assigned an "eccentricity" value, which is calculated as the spectral angle distance between the most spectrally pure and mostly highly mixed pixel for the given spatial neighborhood. This process is repeated iteratively for larger spatial neighborhoods up to a maximum size that is pre-determined. At each iteration the "eccentricity" values of the selected pixels are updated. The final endmember set is obtained by applying a threshold to the resulting greyscale "eccentricity" image. The final endmembers are extracted after a region growing process.

- The spatial spectral endmember extraction (SSEE)[8] algorithm comprises four steps. First, it applies singular value decomposition (SVD) to determine a set of eigenvectors that describe most of the spectral

variance of image subsets. Then, it projects the entire image data onto the compiled eigenvector set to determine a set of candidate endmember pixels. In a third step, the algorithm analyzes the spatial and spectral characteristics of the candidate endmember set to average spectrally similar endmember candidates that are spatially related. Finally, the endmember set derived in the previous step is reordered based on spectral angle, thus listing endmember candidates in order of spectral similarity (from highest to lowest similarity).

3. OVERVIEW OF JPEG2000

The JPEG2000 standard is divided into several and incremental parts. Part 1[18] defines the core coding system and two basic image file formats. Part 2[19] specifies a set of extensions to the core coding system, such as spectral (inter-component) decorrelation and the use of different wavelet kernels, as well as a more extensible file format. These two first parts are the ones we are going to focus on along this paper. The rest of parts introduce some extensions for different applications. For example, Part 10 (named also JP3D)[20] is concerned with the coding of three-dimensional (3D) data. However, this paper is not tackling this part since it is specifically oriented to volumetric (not only multicomponent) "images".

Fig. 1 shows an overview of the data partitioning made by the core coding system of JPEG2000, and how the elements of a three-component image (such as a color RGB image) are encoded and distributed. The first step in the JPEG200 algorithm, not shown in the figure, is a level offset to guarantee that all the samples are signed. This is a requirement of the transform machinery that is going to be applied. After that, a CT (Component Transform, for example, a RGB to a YUV color transform) removes the inter-component redundancy that could be found in the image. The result of this stage is a new image in other domain, with the same number of components and samples per component. Next, as can be observed in the figure, each component of the image is divided into rectangular areas called tiles. Tiling is useful for compound images because the encoding parameters of each tile can be selected taking into account its characteristics. However, the tiling is rarely used in natural images due to the artifacts produced around the edges of the tiles, having commonly only one tile per component.

JPEG2000 allows the use of different decomposition patterns in the component domain, although the default one is the hybrid scheme (see Fig. 2). In the hybrid decomposition, a dyadic 1D-DWT (Discrete Wavelet Transform) is first applied to the component domain. After the inter-component decorrelation stage (CT), the dyadic 2D-DWT (denoted only by DWT in the rest of this paper) is applied to each tile-component. Currently, the DWT is widely used in the processing of scalable image contents because it facilitates the resolution scalability and improves the encoding efficiency, removing the intra-component (spatial) redundancy. In the example of Fig. 1 we can see how four different resolution levels are generated (remarked in black) when a DWT of three iterations is applied to a tile. These resolution levels are commonly referred by positive integer numbers starting from 0 for the highest one, the original image size.

JPEG2000 provides two working paths: a lossy mode and a lossless mode. The main difference between them is the higher encoding performance of the lossy one especially at very low bit-rates due to the higher linearity of

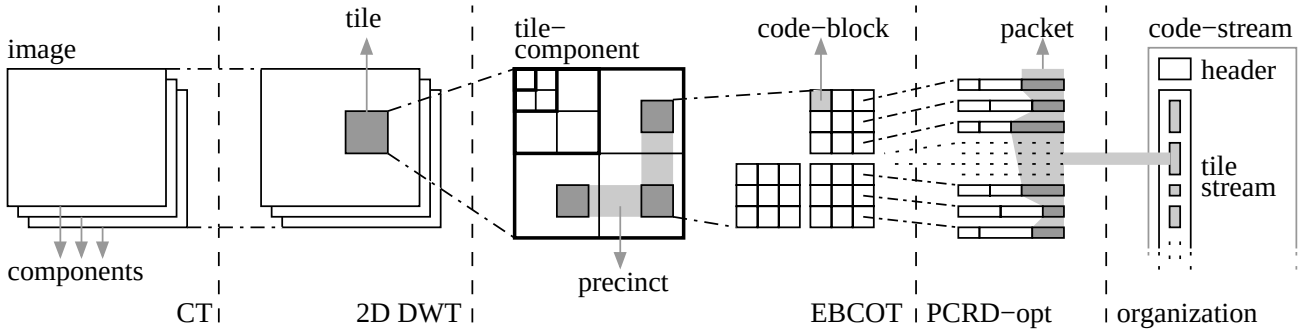

Figure 1. JPEG2000 data partitioning, coding and code-stream organization.

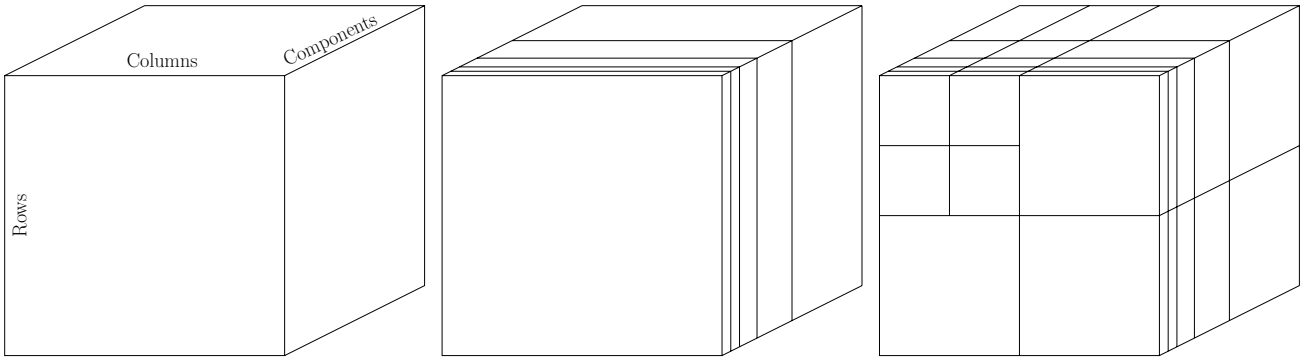

Figure 2. The hybrid scheme for 3D decorrelation. 5 levels for the CT and 2 levels for the DWT.

floating point implementation of the DWT. When no loss of information is allowed, the lossless mode should be selected. A fixed point (integer) version of the DWT is used in this case.

The resultant wavelet coefficients are grouped into rectangular areas (e.g. 64×64 coefficients) called code-blocks, that are encoded independently by the EBCOT[21] (Embedded Block Coding with Optimal Truncation) algorithm. In order to manage the image information more easily, the code-blocks related to the same rectangular location, within the same resolution level, are grouped into precincts. ROI (Region Of Interest) and the spatial scalabilities are achieved in JPEG2000 by means of the precincts. The compressed bit-streams of the code-blocks can be divided into a specific number of contiguous segments, or quality layers, by the PCRD-opt (Post-Compression Rate-Distortion Optimization) rate-allocation algorithm. The segments of all the code-blocks of a precinct associated to the same quality layer are stored as a packet. The packet is the storing unit in JPEG2000 and it is associated to a quality layer (L), a precinct (P), a resolution level (R), and a tile-component (C). A word formed by this four letters specifies the progression order used to store the image packets, existing five different possibilities: LRCP, RLCP, RPCL, PCRL and CPRL.

The LRCP progression allows an incremental quality reconstruction of the image depending on the amount of decoded data. The use of each new packet decreases the distortion of the decoded image at a receiver, providing a fine-grain quality scalability mode. A sequentially decoded RLCP or RPCL image will produce a reconstruction of incremental resolution. The PCRL progression is useful in scan-based systems, like printers. Finally, an CPRL compressed image will be restored, component by component.

The most basic file format defined in the standard, in Part 1, contains only the code-stream of an image (see Fig. 1). This is composed by all the packets of the image and a set of markers with additional information. Although there can be markers in any place of the code-stream, the main ones are included within the header. The image files with this format usually have the extension J2C or J2K.

In order to allow to include more information related to the image apart from just the code-stream, like for example color palettes or meta-data, Part 1 also defines a more complex file format based on "boxes". All the information is organized in boxes, contiguous segments of data, whose content is identified by a four-bytes code in its header. It is possible to define a complex hierarchical structure since a box can contain many other sub-boxes. The extension used to identify the image files with this extension is JP2. In this kind of files, the code-stream, without the header, is stored within a box.

The box-based structure of the JP2 format is extensible. Just defining new four-bytes identifiers would allow to include new kind of boxes within an image file, maintaining the backward compatibility (an image outdated viewer that does not understand certain box codes it just ignores them and processing the others). Part 2 defines a new set of boxes with additional and powerful functionalities. For instance, multiple code-streams may be included within a file, as well as a complex composition scheme (animations, transparency masks, geometric transformations, user definable wavelet kernels, multi-component processing (CT), etc.), in order to control how

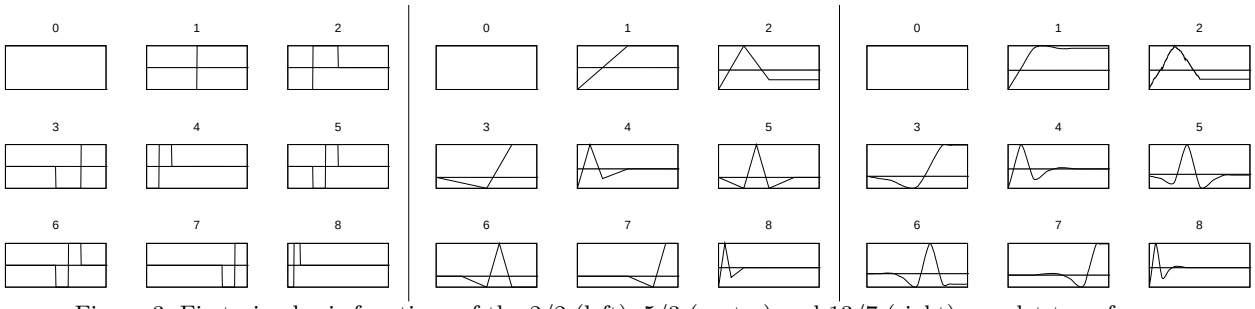

Figure 3. First nine basis functions of the 2/2 (left), 5/3 (center) and 13/7 (right) wavelet transforms.

the image viewer has to show them. The extension JPX is used to identify those files that contain boxes of Part 2. This is the file format for the images of our experiments.

4. THE USED WAVELET FILTERS

Any DWT can be described by its analysis filters, and any inverse DWT by means of its synthesis filters. Wavelet filters (or wavelet kernels) define in a significant way the behavior and the efficiency of the JPEG2000 encoding system. In our work we have investigated the 2/2 (or Haar) kernel,[22] the spline 5/3 (or lineal) kernel,[23] and the spline 13/7 (or cubic) kernel.[24] All of these transforms are based on two-channel filter banks. The notation x/y indicates that the underlining filter bank has lowpass and highpass analysis filters of lengths x and y, respectively.

The analysis filters of the 2/2 transform correspond to

$$\begin{aligned} H_i &= S_{2i+1} - S_{2i} \\ L_i &= S_{2i} + \frac{H_i}{2}, \end{aligned}$$

the analysis filters of the 3/5 transform are

$$\begin{aligned} H_i &= S_{2i+1} - \frac{S_{2i} + S_{2i+2}}{2} \\ L_i &= S_{2i} + \frac{H_{i-1} + H_i}{4}, \end{aligned}$$

and finally, the 13/7 transform have the filters

$$\begin{aligned} H_i &= S_{2i+1} - \Big(\frac{9}{16}\big(S_{2i} + S_{2i+2}\big) - \frac{1}{16}\big(S_{2i-2} + S_{2i+4}\big)\Big) \\ L_i &= S_{2i} + \frac{9}{32}\big(H_{i-1} + H_i\big) - \frac{1}{32}\big(H_{i-2} + H_{i+1}\big), \end{aligned}$$

where S_i denotes the i-th sample of the signal one-dimensional S, L_i the i-th sample of the lowpass subband and H_i the i-th sample of the highpass subband.

Such transforms are linear and have linear phase. As can be observed, it has been expressed using Lifting[25] and are invertible in finite-precision arithmetic (i.e., reversible). Ecuations for the inverse transformation can be easily deduced easily from the forward equations. For the 2D case, the transform is separable. Therefore, images are handled by transforming all the rows and next, all the columns, or viceversa. This step produces four 2D subband named LL, HL, LH y HH. The recursive aplication of this step to the LL subband generates the dyadic 2D DWT. Symmetric extension[26] is used to process the image boundaries.

To finalize the description of the used DWTs, notice that the shape of the basis functions of these transforms has a great importance because it will determine the type of signals for which the transform is effective, and the nature of the artifacts obtained in lossy reconstructions. As can be seen in Fig. 3, the 2/2 transform will generate piecewise reconstructions, the 5/3 transform will produce linear approximations of the original signal and the 13/7 transform smooth reconstructions. For natural images that are composed of a collection of continuous signals, the 13/7 should produce the best results, from a numerical and a visual point of view.

5. EXPERIMENTAL RESULTS

Before describing our numerical results, we first briefly describe the hyperspectral scene used in our experiments. Our reference data set in this study is the well-known AVIRIS Cuprite data set, available online in reflectance units* after atmospheric correction. This scene has been widely used to validate the performance of endmember extraction algorithms. The portion used in experiments corresponds to a 350×350-pixel subset of the sector labeled as f970619t01p02_r02_sc03.a.rfl in the online data. The scene comprises 224 spectral bands between 0.4 and 2.5 μm, with full width at half maximum of 10 nm. Prior to the analysis, several bands were removed due to water absorption and low SNR in those bands, leaving a total of 188 reflectance channels to be used in the experiments. The Cuprite site is well understood mineralogically,[27,28] and has several exposed minerals of interest including those used in the USGS library considered for the generation of simulated data sets. Five of these laboratory spectra (*alunite*, *buddingtonite*, *calcite*, *kaolinite* and *muscovite*) convolved in accordance with AVIRIS wavelength specifications, will be used to assess endmember signature purity in this work.

In our experiments, the images are encoded progressively (lossy-to-lossless) using the reversible path and 20 quality layers. Each quality layer occupies 0.1 bpppb (bit per pixel per band). Therefore, the image reconstructed with the lowest quality is decoded at 0.1 bpppb and the highest quality one is restored using 2.0 bpppb. The progression order selected for the packets is LRCP, producing a progression of incremental quality reconstructions (one for each tested bit-rate). The number of precincts per resolution level is 1, minimizing the number of packets and therefore, minimizing the overhead of the headers of these packets. The code-block size is 64×64 (the maximun allowed). Resilience data, such as SOP or EPH markers, has not been included. Finally, tiling has not been used.

The first set of experiments measures the distortion in terms of the Peak Signal to Noise Ratio (PSNR) as a funtion of the bit-rate, the type of wavelet filter used in the DWT and the number of levels of the CT and the DWT. As can be seen in Fig. 4, the encoding performance increases with the number of levels of the CT, the number of levels of the DWT and the length of the filters. To measure the impact of there parameters, we have tested the extreme cases (0 and 8 levels for the CT; 0 and 5 levels for the DWT, althought a 1-level DWT has been also tested) for all filters. These extreme cases have been selected empirically, minimizing the distortion. From these results it can be concluded that the inter-component redundancy is much higher that the intra-component redundancy in the image. This is the main factor to be taken in account. After that, the number of levels of the DWT has a medium impact on the performance. Finally, the length of the filter is the less relevant parameter.

The second set of experiments measures the impact of compression on the quality of the endmembers extracted by the AMEE and SSEE methods and on the fractional abundances estimated using such methods. The quality of extracted endmember pixels from the original and/or reconstructed images is measured by the spectral angle distance (SAD) measured between corresponding pixels in the two images. SAD is a well known metric for hyperspectral data processing[4] and can be used to measure the spectral similarity between two pixel vectors, $\mathbf{X}(i,j)$ and $\mathbf{X}(r,s)$, as follows:

$$\gamma = \mathrm{SAD}(\mathbf{X}(i,j), \mathbf{X}(r,s)) = \cos^{-1} \frac{\mathbf{X}(i,j) \cdot \mathbf{X}(r,s)}{\|\mathbf{X}(i,j)\| \|\mathbf{X}(r,s)\|}. \quad (2)$$

It should be noted that SAD is given by the cosine of the spectral angle formed by n-dimensional vectors. As a result, this metric is invariant in the multiplication of $\mathbf{X}(i,j)$ and $\mathbf{X}(r,s)$ by constants and, consequently, is invariant before unknown multiplicative scalings that may arise due to differences in illumination and angular orientation.[4]

On the other hand, the quality of fractional abundances estimated from the original and/or reconstructed images is measured by assuming that a set of high-quality endmembers (and their corresponding estimated abundance fractions) may allow reconstruction of a hyperspectral scene [by means of Eq. (1)] with highest precision than a set of low-quality endmembers. Let us assume that $\mathbf{I}^{(\mathrm{O})}$ is a hyperspectral scene, and that $\mathbf{I}^{(\mathrm{R})}$ is a reconstructed version of $\mathbf{I}^{(\mathrm{O})}$, obtained using Eq. (1) with a set of endmembers, automatically derived by

*http://aviris.jpl.nasa.gov/html/aviris.freedata.html

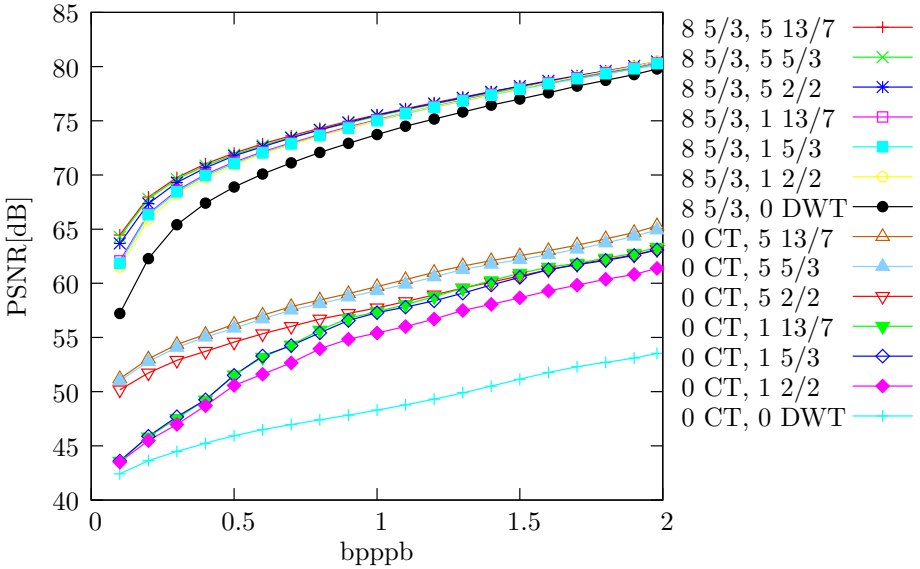

Figure 4. PSNR (expresed in decibels) versus the bit-rate (expresed in bits per pixel per band) for a progressive in quality reconstruction of the AVIRIS Cuprite image.

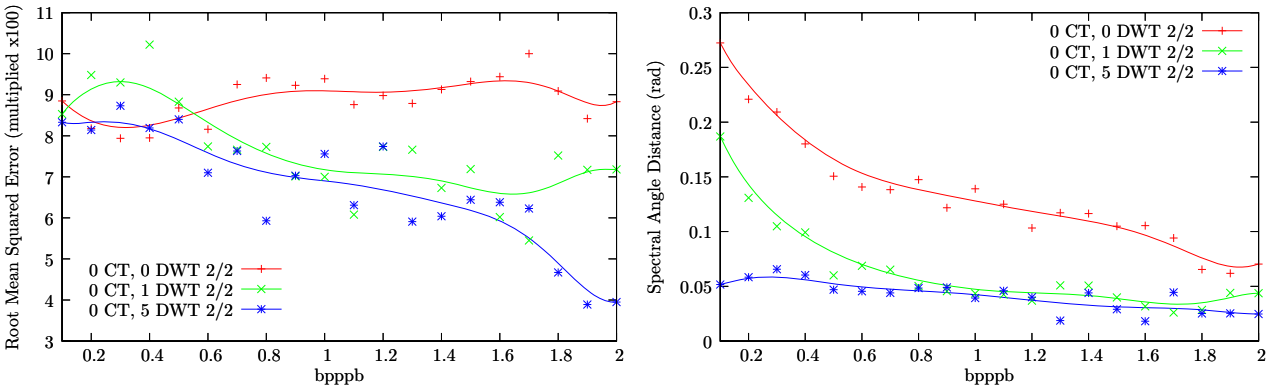

Figure 5. 2x2-AMEE-RMSE (left), 2x2-AMEE-SAD (right).

a certain algorithm from the original scene, and their corresponding fractional abundances. Let us also assume that the pixel vector at spatial coordinates (i,j) in the original hyperspectral scene is given by $\mathbf{X}^{(\mathrm{O})}(i,j) = [x_1^{(\mathrm{O})}(i,j), x_2^{(\mathrm{O})}(i,j), \cdots, x_n^{(\mathrm{O})}(i,j)]$, while the corresponding pixel vector at the same spatial coordinates in the reconstructed hyperspectral scene is given by $\mathbf{X}^{(\mathrm{R})}(i,j) = [x_1^{(\mathrm{R})}(i,j), x_2^{(\mathrm{R})}(i,j), \cdots, x_n^{(\mathrm{R})}(i,j)]$. With the above notation in mind, the RMSE between the original and the reconstructed hyperspectral scenes is calculated as follows:

$$\mathrm{RMSE}(\mathbf{I}^{(\mathrm{O})}, \mathbf{I}^{(\mathrm{R})}) = \frac{1}{s \times l} \sum_{i=1}^{s} \sum_{j=1}^{l} \left(\frac{1}{n} \sum_{k=1}^{n} [x_k^{(\mathrm{O})}(i,j) - x_k^{(\mathrm{R})}(i,j)]^2 \right)^{\frac{1}{2}}. \quad (3)$$

With the above definitions in mind, Figs. 5 and 6 respectively show the SAD and RMSE-based scores for the AMEE and SSEE algorithms using Haar as the wavelet kernel. Here, the SAD-based scores correspond to the average of the spectral angles obtained for the five considered minerals (*alunite*, *buddingtonite*, *calcite*, *kaolinite*, and *muscovite*) while the RMSE-based scores correspond to per-pixel comparisons between the fractional abundances obtained for the original versus the compressed scenes. On the other hand, Figs. 7 and 8 respectively

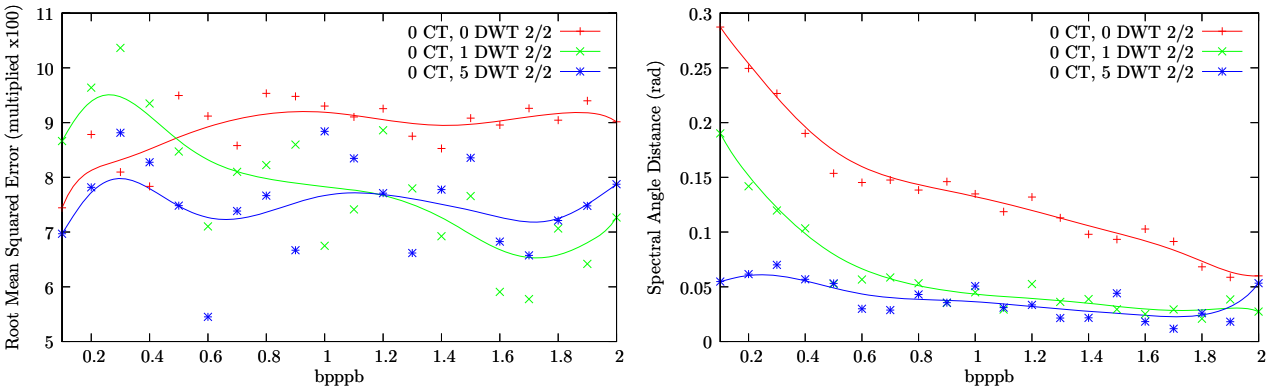

Figure 6. 2x2-SSEE-RMSE (left), 2x2-SSEE-SAD (right).

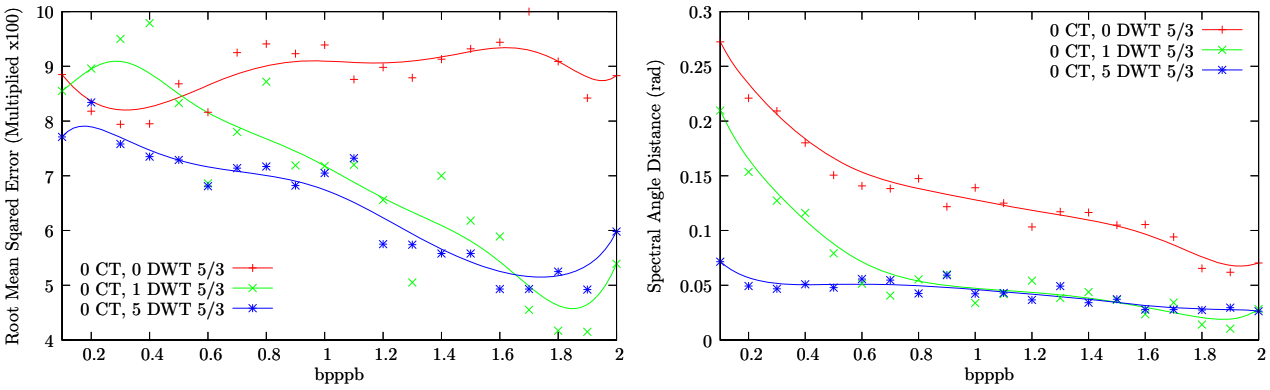

Figure 7. 5x3-AMEE-RMSE (left), 5x3-AMEE-SAD (right).

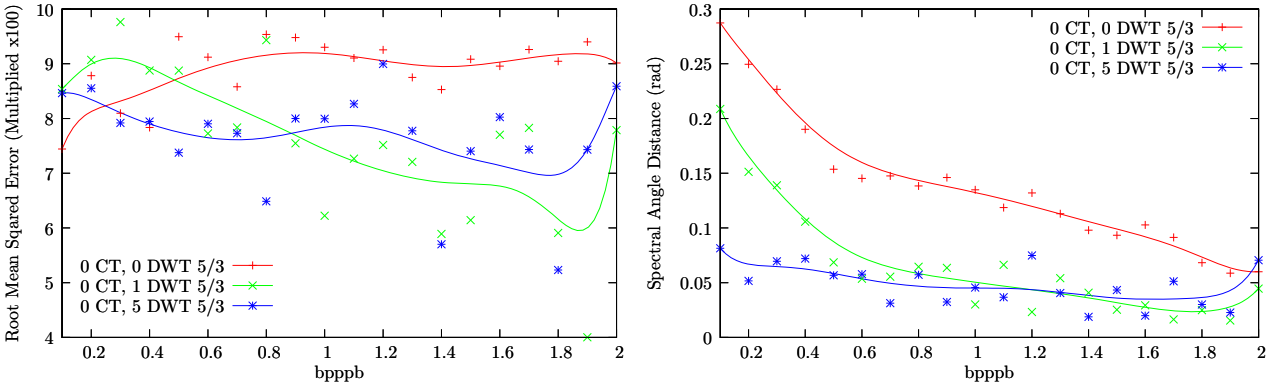

Figure 8. 5x3-SSEE-RMSE (left), 5x3-SSEE-SAD (right).

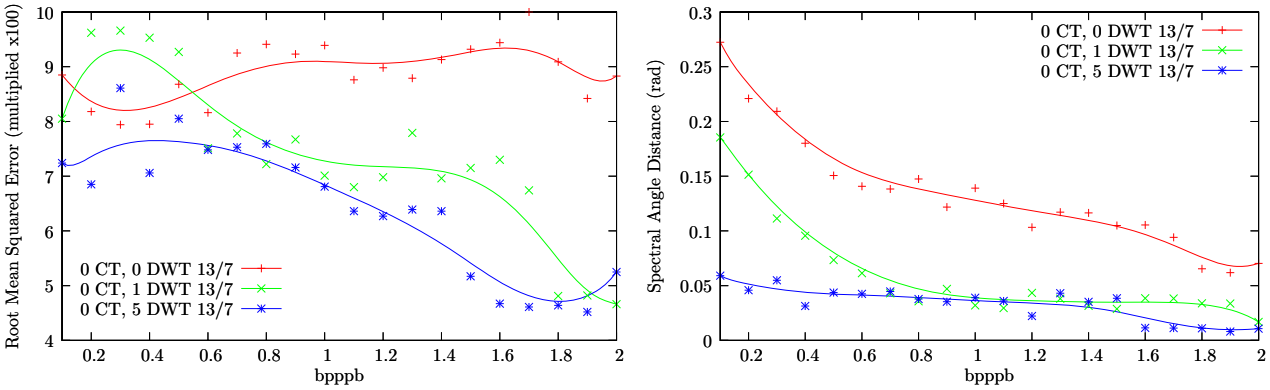

Figure 9. 13x7-AMEE-RMSE (left), 13x7-AMEE-SAD (right).

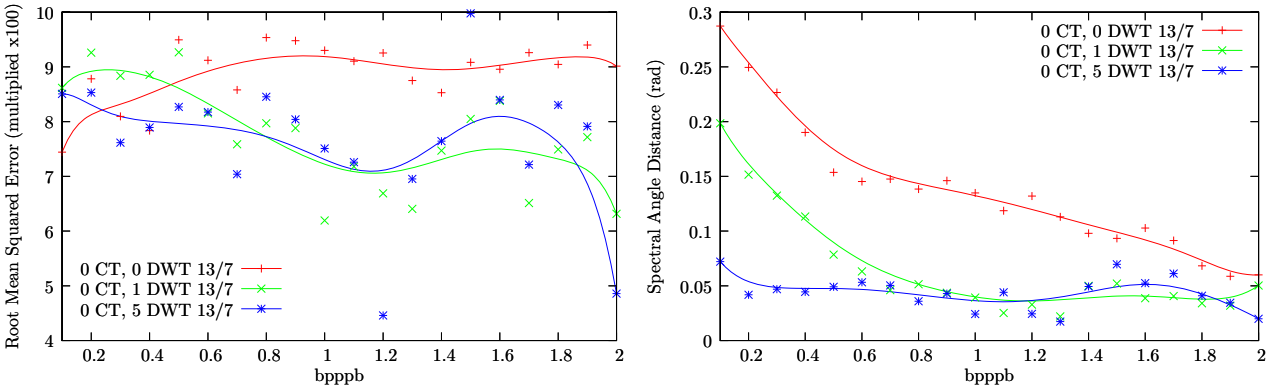

Figure 10. 13x7-SSEE-RMSE (left), 13x7-SSEE-SAD (right).

show the same using the lineal kernel. Finally, Figs. 9 and 10 respectively show the same scores using the cubic kernel. From this set of figures, it can be seen that the SAD-based metric seems to be more sensitive to the number of levels used in the DWT decomposition for the images reconstructed with lower quality (low bpppb) values. As the number of quality layers increases, similar results are obtained by both AMEE and SSEE algorithms. Quite opposite, the RMSE-based metric is affected by both parameters, i.e., the number of levels and the number of layers, with both AMEE and SSEE providing better results for 5 DWT levels as the bpppb increases. In contrast, when 0 DWT levels are used, both algorithms perform similarly regardless of the number of layers.

A detailed inter-comparison of AMEE and SSEE algorithm revels that, despite both algorithms perform similarly in all considered tests (which is a very interesting result since the strategies used to incorporate spatial information into endmember extraction are very different in both cases), the AMEE seems to provide more consistent results while SSEE often provides peaks and valleys in the SAD and RMSE plots versus the bpppb values. This is probably due to the fact that SSEE does not simultaneously integrate the spatial and the spectral information when searching for image endmembers (the algorithm is based on an SVD-based spectral procedure followed by spatial averaging). However, the extended morphological operations used for the implementation of AMEE jointly consider the two sources of information (spatial and spectral) when searching for endmembers and without giving more priority to one of the sources versus the other, which apparently provides more stable results in terms of the sensitivity of the algorithm to different parameters tested. Further experimentation should be conducted in future work in order to validate the above remarks on different case studies using additional hyperspectral scenes and spatial-spectral endmember extraction algorithms. Despite our analysis in this work is confined to two algorithms only, these approaches are among the most representative ones in the recent endmember extraction literature and the experimental findings reported in this work will be of interest

to practitioners interested in applying those algorithms to hyperspectral images with different quality levels resulting from lossy compression.

6. CONCLUSIONS AND FUTURE RESEARCH LINES

The wealth of spatial and spectral information provided by hyperspectral imaging instruments is essential in many applications, and in many cases needs to be retained by compression algorithms with a high degree of fidelity. In this paper, we have evaluated the impact of lossy, JPEG2000-based hyperspectral data compression on spectral unmixing applications, with particular attention on spatial-spectral endmember extraction using two recently proposed algorithms. Our experiments reveal that the performance of endmember extraction algorithms using both spatial and spectral information, such as AMEE or SSEE, is quite similar in the presence of different parameters such as compression ratio, number of levels used in the DWT or type of kernel used, despite the fact that both algorithms use very different strategies to incorporate spatial information into the endmember extraction process. A detailed inter-comparison of both algorithms indicates that the AMEE provides slightly more robust results in terms of the SAD-based quality of the endmembers extracted and the RMSE-based quality of the associated fractional abundances. This may be due to the fact that the AMEE considers jointly the spatial and the spectral information (without prioritizing any of them) during the endmember searching process, while the SSEE first uses a spectral-based procedure followed by spatial averaging and, thus, the two sources of information are not treated simultaneously. Our investigation of the maximum compression ratio that can be achieved without compromising the quality of the endmembers extracted by different algorithms will be continued in future research by incorporating additional hyperspectral scenes and spatial-spectral endmember extraction algorithms to the comparison. This study may be useful to image analysts interested in assessing the impact of lossy compression on spectral mixture analysis applications that jointly use the spatial and the spectral information in the analysis.

ACKNOWLEDGEMENT

This work has been supported by the European Community's Marie Curie Research Training Networks Programme under reference MRTN-CT-2006-035927, Hyperspectral Imaging Network (HYPER-I-NET). Funding from the Spanish Ministry of Science and Innovation (HYPERCOMP/EODIX project, reference AYA2008-05965-C04-02) is also gratefully acknowledged, and it has been supported by grant TIN2008-01117 (Spanish Ministry of Science and Innovation).

REFERENCES

[1] Motta, G., Rizzo, F., and Storer, J. A., [*Hyperspectral data compression*], Springer-Verlag, New York (2006).

[2] Green, R. O., Eastwood, M. L., Sarture, C. M., Chrien, T. G., Aronsson, M., Chippendale, B. J., Faust, J. A., Pavri, B. E., Chovit, C. J., Solis, M., et al., "Imaging spectroscopy and the airborne visible/infrared imaging spectrometer (AVIRIS)," *Remote Sensing of Environment* **65**(3), 227–248 (1998).

[3] Du, Q. and Chang, C.-I., "Linear mixture analysis-based compression for hyperspectral image analysis," *IEEE Transactions on Geoscience and Remote Sensing* **42**, 875–891 (2004).

[4] Keshava, N. and Mustard, J. F., "Spectral unmixing," *IEEE Signal Processing Magazine* **19**(1), 44–57 (2002).

[5] Adams, J. B., Smith, M. O., and Johnson, P. E., "Spectral mixture modeling: a new analysis of rock and soil types at the Viking Lander 1 site," *Journal of Geophysical Research* **91**, 8098–8112 (1986).

[6] Plaza, A., Martinez, P., Perez, R., and Plaza, J., "A quantitative and comparative analysis of endmember extraction algorithms from hyperspectral data," *IEEE Transactions on Geoscience and Remote Sensing* **42**(3), 650–663 (2004).

[7] Plaza, A., Martinez, P., Perez, R., and Plaza, J., "Spatial/spectral endmember extraction by multidimensional morphological operations," *IEEE Transactions on Geoscience and Remote Sensing* **40**(9), 2025–2041 (2002).

[8] Rogge, D. M., Rivard, B., Zhang, J., Sanchez, A., Harris, J., and Feng, J., "Integration of spatial–spectral information for the improved extraction of endmembers," *Remote Sensing of Environment* **110**(3), 287–303 (2007).

[9] Taubman, D. S. and Marcellin, M. W., [*JPEG2000: Image compression fundamentals, standard and practice*], Kluwer, Boston (2002).

[10] Heinz, D. and Chang, C.-I., "Fully constrained least squares linear mixture analysis for material quantification in hyperspectral imagery," *IEEE Transactions on Geoscience and Remote Sensing* **39**, 529–545 (2001).

[11] Boardman, J. W., Kruse, F. A., and Green, R. O., "Mapping Target Signatures Via Partial Unmixing of Aviris Data," *Proc. JPL Airborne Earth Sci. Workshop* , 23–26 (1995).

[12] Winter, M. E., "N-FINDR: an algorithm for fast autonomous spectral end-member determination in hyperspectral data," *Proc. SPIE Image Spectrometry V* **3753**, 266–277 (2003).

[13] Neville, R. A., Staenz, K., Szeredi, T., Lefebvre, J., and Hauff, P., "Automatic endmember extraction from hyperspectral data for mineral exploration," *Proc. 21st Canadian Symp. Remote Sens.* , 21–24 (1999).

[14] Bowles, J. H., Palmadesso, P. J., Antoniades, J. A., Baumback, M. M., and Rickard, L. J., "Use of filter vectors in hyperspectral data analysis," *Proc. SPIE Infrared Spaceborne Remote Sensing III* **2553**, 148–157 (1995).

[15] Ifarraguerri, A. and Chang, C.-I., "Multispectral and hyperspectral image analysis with convex cones," *IEEE Transactions on Geoscience and Remote Sensing* **37**(2), 756–770 (1999).

[16] Harsanyi, J. C. and Chang, C.-I., "Hyperspectral image classification and dimensionality reduction: An orthogonal subspace projection," *IEEE Transactions on Geoscience and Remote Sensing* **32**(4), 779–785 (1994).

[17] Plaza, A., Martinez, P., Plaza, J., and Perez, R., "Dimensionality reduction and classification of hyperspectral image data using sequences of extended morphological transformations," *IEEE Transactions on Geoscience and Remote Sensing* **43**(3), 466–479 (2005).

[18] International Organization for Standardization, "Information Technology - JPEG2000 Image Coding System - Part 1: Core Coding System." ISO/IEC 15444-1:2004 (2004).

[19] International Organization for Standardization, "Information Technology - JPEG2000 Image Coding System - Part 2: Extensions." ISO/IEC 15444-2:2004 (2004).

[20] International Organization for Standardization, "Information technology - JPEG2000 image coding system: Extensions for three-dimensional data." ISO/IEC 15444-10:2008 (2008).

[21] Taubman, D., "High performance scalable image compression with EBCOT," *IEEE Transactions on Image Processing* **9**(7), 1158–1170 (2000).

[22] Haar, A., "Zur Theorie der orthogolanen Funktionen-Systeme," *Mathematische Annalen* **69**, 331–371 (1910).

[23] Gall, D. L. and Tabatabai, A., "Sub-band coding of digital images using sysmmetric short kernel filters and arithmetic coding techniques," in [*Proc. IEEE Int. Conf. Acoustics, Speech and Signal Processing*], **2**, 761–764 (April 1988).

[24] Strang, G. and Nguyen, T., [*Wavelets and Filter Banks*], Wellesley-Cambridge Press (1996).

[25] Sweldens, W., "The Lifting Scheme: A new Philosophy in Biorthogonal Wavelet Constructions," in [*Proc. SPIE*], **2569**, 68–79 (September 1995).

[26] Brislawn, C. M., "Preservation of Subband Symmetry in Multirate Signal Coding," *IEEE Trans. Signal Process.* **43**, 3046–3050 (December 1995).

[27] Clark, R. N., Swayze, G. A., Livo, K. E., Kokaly, R. F., Sutley, S. J., Dalton, J. B., McDougal, R. R., and Gent, C. A., "Imaging spectroscopy: Earth and planetary remote sensing with the usgs tetracorder and expert systems," *Journal of Geophysical Research* **108**, 1–44 (2003).

[28] Swayze, G., Clark, R. N., Kruse, F., Sutley, S., and Gallagher, A., "Ground-truthing AVIRIS mineral mapping at Cuprite, Nevada," *Proc. JPL Airborne Earth Sci. Workshop* , 47–49 (1992).